
Molecular and Atomic Clouds toward NGC 2359: Evidence for Isolated Wolf-Rayet Star Formation Triggered by a Cloud-Cloud Collision

Hidetoshi SANO^{1,2}, Kazufumi TORII³, Shun SAEKI², Kazuki OKAWA²,
Kisetsu TSUGE², Daichi TSUTSUMI², Mikito KHONO², Yusuke
HATTORI², Shinji FUJITA², Satoshi YOSHIKE², Rei ENOKIYA², Ryuji
OKAMOTO², Katsuhiko HAYASHI², Atsushi NISHIMURA², Akio
OHAMA², Takahiro HAYAKAWA², Hiroaki YAMAMOTO², Kengo
TACHIHARA², Cristina Elisabet CAPPA^{4,5} and Yasuo FUKUI^{1,2}

¹Institute for Advanced Research, Nagoya University, Furo-cho, Chikusa-ku, Nagoya
464-8601, Japan

²Department of Physics, Nagoya University, Furo-cho, Chikusa-ku, Nagoya 464-8601, Japan

³Nobeyama Radio Observatory, Minamimaki-mura, Minamisaku-gun, Nagano 384-1305,
Japan

⁴Instituto Argentino de Radioastronomía, CONICET, Argentina.

⁵Facultad de Ciencias Astronómicas y Geofísicas, Universidad Nacional de la Plata, Paseo
del Bosque s/n, 1900, La Plata, Argentina.

*E-mail: sano@a.phys.nagoya-u.ac.jp

Received ; Accepted

Abstract

NGC 2359 is an HII region located in the outer Galaxy that contains the isolated Wolf-Rayet (WR) star HD 56925. We present new CO observations of NGC 2359 with the Nobeyama 45-m radio telescope and the Atacama Submillimeter Telescope Experiment using the $^{12}\text{CO}(J = 1-0, 3-2)$ emission lines and compare them with archived H α and radio-continuum data from the Very Large Array. Our purpose is to investigate whether the formation of the WR star in

NGC 2359 was triggered by a cloud-cloud collision. We find two molecular clouds at ~ 37 and ~ 54 km s $^{-1}$, and two H I clouds at ~ 54 and ~ 63 km s $^{-1}$. All are likely to be associated with NGC 2359 as suggested by good morphological correspondence not only with an optical dark lane through the nebula but also with the radio-shell boundary. We also find that the molecular cloud at ~ 54 km s $^{-1}$ has a high kinematic temperature of at least ~ 40 K, thus indicating that the gas temperature has been increased because of heating by the WR star. We propose that both NGC 2359 and the isolated WR star were created by a collision between the two molecular clouds. The supersonic velocity separation of the two clouds cannot be explained by stellar feedback from the WR star. The complementary spatial distributions and bridging features of CO and H I also are in good agreement with the expected observational signatures of high-mass star formations triggered by cloud-cloud collisions. We argue that NGC 2359 may be in the final phase of a cloud-cloud collision and that the collision timescale is ~ 1.5 Myr or longer. We also note that there is no significant difference between the physical properties of colliding clouds that trigger the formation of isolated O-type and WR stars.

Key words: ISM: H II regions—Stars: formation—ISM: individual objects (NGC 2359)

1 Introduction

It is a longstanding question how isolated (or so-called “field”) high-mass stars are formed in interstellar space. Recently, the cloud-cloud collision model has received considerable attention as a formation mechanism not only for high-mass stellar clusters but also for isolated high-mass stars. Torii et al. (2011, 2017a) showed that the isolated O-type star associated with the H II region M20 was formed by a collision between two molecular clouds, that have a velocity separation of ~ 8 km s $^{-1}$. They detected a high intensity ratio (> 1) of CO $J = 3-2 / 1-0$ toward both clouds, thus suggesting a physical association with the O-type star. They also found that the two clouds have complementary spatial distributions and that a bridging feature physically connects the two clouds in velocity space. On the basis of comparisons with numerical simulations, they concluded that the complementary spatial distributions and the bridging feature can be interpreted as typical cloud-cloud collision signatures. Therefore, the isolated O-type star in M20 is not a runaway star but was formed by strong gas compression during the cloud-cloud collision.

Theoretical studies also support this idea because a collision between two dense clouds

increases the effective sound speed and gas density in the shocked layer (e.g., Habe & Ohta 1992; Anathpindika 2010; Inoue & Fukui 2013; Takahira et al. 2014; Inoue et al. 2017). According to Inoue et al. (2017), isothermal magnetohydrodynamic simulations of cloud-cloud collisions can achieve high accretion rates $M_{\text{acc}} > 10^{-4} M_{\odot} \text{ yr}^{-1}$, which is high enough to allow the formation of O-type stars (e.g., Wolfire & Cassinelli 1987). They also found that the most massive sink particle, which has a mass of $50 M_{\odot}$ or higher, was created within a few 10^5 yr after the collision.

To date, observational evidence for cloud-cloud collisions as a formation mechanism for O-type stars has been obtained from 22 sources associated with stellar clusters containing 2 or more O-type stars (Hasegawa et al. 1994; Furukawa et al. 2009; Ohama et al. 2010, 2017; Fukui et al. 2014, 2016; 2017a; 2017b; 2017c; 2017d; 2017e; Tsuboi et al. 2015; Voisin et al. 2016; Dewangan 2017; Kohno et al. 2017; Nishimura et al. 2017a, 2017b; Torii et al. 2017b, 2017c; Sano et al. 2017; Okawa et al. 2017; Tsuge et al. 2017; Fujita et al. 2017) and with 5 sources associated with isolated high-mass stars (Torii et al. 2011, 2015, 2017a; Fukui et al. 2015; Saigo et al. 2017; Hayashi et al. 2017).

However, isolated Wolf-Rayet (WR) stars have not previously been studied as products of star formation triggered by the cloud-cloud collisions. A WR star is thought to be a late evolutionary stage of an O-type star with a mass of $\sim 25 M_{\odot}$ or higher. WR stars have lost their hydrogen envelopes via strong stellar winds, with typical velocities and mass-loss rates of $\sim 1000 \text{ km s}^{-1}$ to 3000 km s^{-1} and $\sim 10^{-5} M_{\odot} \text{ yr}^{-1}$, respectively (e.g., Crowther 2007 and references therein). To advance our knowledge of the formation of isolated high-mass stars, we need to clarify whether the formation of isolated WR stars may have been triggered by a cloud-cloud collisions.

NGC 2359 (also known as Sh 2–298 or Thor’s Helmet) is an optical ring nebula associated with the isolated WR star HD 56925 (= WR 7, van der Hucht et al. 1981). Figure 1 shows an optical image of NGC 2359 (courtesy of Robert Franke) obtained at the Focal Pointe Observatory. The WR star is categorized as spectral type WN4b (Smith et al. 1996) and is located at $(l, b) \sim (227^{\circ}750, -0^{\circ}129)$. It has formed a wind-blown bubble that is ~ 4.5 in diameter. By using the interferometric profiles of $\text{H}\alpha$, [OIII], and [NII], the expansion velocity of the bubble was found to range from $\sim 15 \text{ km s}^{-1}$ to 30 km s^{-1} (Schneps et al. 1981; Treffers & Chu 1982; Goudis et al. 1983; Goudis et al. 1994; Meaburn et al. 1994) up to $55 \pm 25 \text{ km s}^{-1}$ (Lozinskaya 1973). The nebula also contains a number of optical/radio filaments corresponding to diffuse ionized gas. Furthermore, two prominent optical dark lanes are located at $(l, b) \sim (227^{\circ}82, -0^{\circ}13)$ and $(227^{\circ}77, -0^{\circ}07)$.

The distance to the nebula and the WR star is still a matter of debate. The photometric distance to HD 56925 was determined to be $\sim 3.5 \text{ kpc}$ to 6.9 kpc (Smith 1968; Crampton 1971; van der Hucht 2001), whereas the kinematic distance to NGC 2359 was found to be $4.0\text{--}6.3 \text{ kpc}$ according to the radial velocity of the CO and optical lines (Georgelin et al. 1973; Peimbert et al. 1978; Talent &

Dufour 1979; Fich & Blitz 1984). In the present study, we adopt an average distance of ~ 5 kpc, following the same assumptions as in previous studies (e.g., Cappa et al. 2001; Rizzo et al. 2001).

Both CO and HI observations have been reported in the direction of NGC 2359. Schneps et al. (1981) first observed the ^{12}CO and $^{13}\text{CO}(J = 1-0)$ emission lines by using the NRAO 11 m radio telescope, which has an angular resolution $\Delta\theta \sim 1'.1$. They found that there are three velocity components at $V_{\text{LSR}} \sim 37, \sim 54, \text{ and } \sim 67 \text{ km s}^{-1}$. By contrast, Cappa et al. (1999) made a complete observation of HI by using the Very Large Array (VLA) at $\Delta\theta \sim 45''$. They found that the components at $V_{\text{LSR}} \sim 54$ and $\sim 63 \text{ km s}^{-1}$ clearly trace along the optical wind-blown bubble, and they concluded that these HI clouds are associated with NGC 2359. Subsequent follow-up CO($J = 1-0, 2-1$) observations were conducted using the SEST 15 m telescope with a fine angular resolution of $22''-44''$ (Cappa et al. 2001). On the basis of a comparative study of the CO, HI, and optical line emissions, they conclude that the CO and HI components at $V_{\text{LSR}} \sim 54 \text{ km s}^{-1}$ are definitely associated with the nebula. Rizzo et al. (2001) provided further support for this conclusion. By observing the fully-sampled CO($J = 1-0, 2-1$) emission lines via the NRAO 12 m radio telescope ($\Delta\theta = 27''-54''$), they found that the CO cloud shows line broadening $> 5.5 \text{ km s}^{-1}$ and a high kinetic temperature of up to 80 K. Furthermore, Rizzo et al. (2003) determined the detailed physical conditions in the CO cloud at $V_{\text{LSR}} \sim 54 \text{ km s}^{-1}$ by using the IRAM 30 m radio telescope ($\Delta\theta \sim 12''$) with fully sampled CO($J = 1-0, 2-1$) emission lines. They found multi-shocked layers in the CO cloud at $V_{\text{LSR}} = 42-48 \text{ km s}^{-1}, 48-52 \text{ km s}^{-1}, \text{ and } 52-57 \text{ km s}^{-1}$, which may have been formed by several energetic events. However, no high-excitation CO lines were observed, such as CO($J = 3-2$), which can trace high temperature and dense regions. Moreover, no study has determined whether there is a relation between the molecular clouds and formation of the WR star.

In this study, we use new CO($J = 1-0, 3-2$) datasets obtained with the Nobeyama 45 m and Atacama Submillimeter Telescope Experiment (ASTE) radio telescopes to investigate whether the formation of the WR star in NGC 2359 was triggered by a cloud-cloud collision. Section 2 describes the CO observations and other wavelength datasets. Section 3 comprises five subsections. Subsections 3.1 and 3.2 present the large-scale distribution of the interstellar medium and its physical conditions; Subsection 3.3 describes the distributions of molecular and atomic clouds in the direction of NGC 2359; Subsection 3.4 presents the physical condition in the molecular clouds; Subsection 3.5 presents position-velocity diagrams for CO and HI. The discussion and our conclusions are given in Sections 4 and 5, respectively.

2 Observations

2.1 CO

We performed $^{12}\text{CO}(J = 1-0)$ observations from March 2015 to April 2015 by using the Nobeyama 45 m radio telescope, which is operated by Nobeyama Radio Observatory in Japan. We observed an area of ~ 170 arcmin² by using the Nyquist sampled on-the-fly (OTF) mapping mode (Sawada et al. 2008). The front end was the two-beam, waveguide-type, dual-polarization, sideband-separating (2SB) SIS receiver system “TZ1” (Nakajima et al. 2013). The backend system, the Spectral Analysis Machine for the 45 m telescope (SAM45; Kuno et al. 2011; Kamazaki et al. 2012), had 4,096 channels with a bandwidth of 250 MHz, corresponding to a velocity coverage of ~ 650 km s⁻¹ and a velocity resolution of ~ 0.18 km s⁻¹ ch⁻¹. Typical system temperatures were ~ 300 K to 500 K for the H polarization and ~ 400 K to 600 K for the V polarization, including the atmosphere. The data cube was smoothed with a Gaussian kernel and the final beam size was 25". We checked the pointing accuracy every hour to achieve an offset less than 2". We calibrated the absolute intensity by observing Orion-IRC2 [$\alpha_{\text{B1950}} = 5^{\text{h}}32^{\text{m}}47.^{\text{s}}0$, $\delta_{\text{B1950}} = -5^{\circ}24'23.''0$], and the estimated error was $\sim 7\%$. The final noise fluctuation was ~ 0.64 K at a velocity resolution of 0.4 km s⁻¹.

We conducted observations of $^{12}\text{CO}(J = 3-2)$ during November and December 2015 by using the ASTE (Ezawa et al. 2004). We used the Nyquist-sampled OTF mapping mode, and the observation area was ~ 120 arcmin². The front end was the cartridge-type 2SB mixer receiver “DASH 345.” The typical system temperature was ~ 250 K in a single sideband. The back end system “MAC” used for spectroscopy (Sorai et al. 2000), had 1,024 channels with a bandwidth of 128 MHz. The velocity resolution and coverage were ~ 0.11 km s⁻¹ ch⁻¹ and ~ 111 km s⁻¹, respectively. We convolved the data cube with a Gaussian kernel, and the final beam size was $\sim 25''$. The pointing accuracy was checked every hour to achieve an offset within 3". We calibrated the absolute intensity by observing IRC+10216 [$\alpha_{\text{B1950}} = 9^{\text{h}}45^{\text{m}}14.^{\text{s}}8$, $\delta_{\text{B1950}} = -13^{\circ}30'40''$] (Wang et al. 1994), and the estimated error was less than 7%. We obtained a data cube with a noise fluctuation of ~ 0.1 K at a velocity resolution of 0.4 km s⁻¹.

We also used the $^{12}\text{CO}(J = 1-0)$ data, which were obtained with the NANTEN 4 m millimeter/submillimeter radio telescope of Nagoya University at Las Campanas Observatory in Chile. The observations were conducted as part of the NANTEN Galactic Plane CO Survey (Mizuno & Fukui 2004). The telescope had a beam size of 2.6' at a frequency of 115 GHz. The velocity resolution and coverage were 0.5 and 600 km s⁻¹, respectively. In this paper, the beam size to 4' was smoothed. The final noise fluctuation in the data was ~ 0.24 K at a velocity resolution of 0.5 km s⁻¹.

2.2 HI & Radio Continuum

To determine the spatial distributions of atomic hydrogen gas and ionized matter, we used the datasets for HI and for the radio continuum at 1465 MHz that appear in Cappa et al. (1999). The data were obtained using the VLA of the National Radio Astronomy Observatory in April and August 1996. The final beam size was $57''.7 \times 40''.6$ with a position angle of -16° for the HI; $39''.2 \times 24''.9$ with a position angle of -52° for the radio continuum. The velocity coverage and resolution for HI were 164 and 1.3 km s^{-1} , respectively. The typical noise fluctuation was $\sim 0.93 \text{ K}$ at a velocity resolution of 1.3 km s^{-1} for the HI; it was $\sim 0.19 \text{ K}$ for the radio continuum.

To cover the large area of HI around NGC 2359, we also used an archival HI dataset from the third data release of the Parkes Galactic All-Sky Survey (GASS III; Kalberla & Haud 2015)¹. The beam size was $16''.4$. The velocity coverage and resolution were $\sim 1,000 \text{ km s}^{-1}$ and 0.82 K , respectively. The typical noise fluctuation around NGC 2359 was $\sim 0.041 \text{ K}$ at a velocity resolution of $\sim 1.3 \text{ km s}^{-1}$.

2.3 Dust Opacity & Temperature

We used archival datasets for the dust opacity τ_{353} at 353 GHz and for the dust temperature T_d to determine the properties of the interstellar gas around NGC 2359. The angular resolution of these datasets was $\sim 4'$. We utilized the data release version R1.20 (see Planck Collaboration et al. 2014).

3 Results

3.1 Large-scale distribution of the interstellar medium

Figures 2a and 2b show CO and HI maps obtained with NANTEN and Parkes covering $5^\circ \times 5^\circ$ around the WR nebula NGC 2359. The nebula, indicated by the white square, is located in the direction of a low-density region. A prominent giant molecular cloud is located at $(l, b) \sim (226.0, -0.5)$. It is not physically connected with NGC 2359 because of its large separation of $\sim 200 \text{ pc}$ from the nebula. We also note that some other molecular clouds with intensities of $\sim 8 \text{ K km s}^{-1}$ or higher are detected in the large-scale map. The total HI intensity toward the nebula is $\sim 3 \times 10^3 \text{ K km s}^{-1}$.

Figures 2c and 2d show maps of the dust opacity τ_{353} at the frequency of 353 GHz and the dust temperature T_d , as determined by the Planck Collaboration et al. (2014). The maps for CO, $\tau_{353} > 1 \times 10^{-4}$, and $T_d < 17 \text{ K}$ have good spatial correspondence, but the correlation with HI is unclear. Similar trends have been found in previous studies of the high-latitude cloud complexes MBM 53, 54, 55, HLCG 92–35, and Perseus (Fukui et al. 2014; Okamoto et al. 2017). We also find an enhancement

¹ <http://www.astro.uni-bonn.de/hisurvey/>

of T_d in the direction of NGC 2359; this finding indicates heating because of the UV radiation from the WR star.

3.2 $X(\text{CO})$ determination

To investigate the physical conditions of the interstellar gas toward NGC 2359 and its surroundings, we have determined the conversion factor $X(\text{CO})$ between the CO integrated intensity $W(\text{CO})$ and the molecular hydrogen column density $N(\text{H}_2)$. According to Okamoto et al. (2017), the total interstellar hydrogen column density N_{H} is given by;

$$N_{\text{H}} = 9.0 \times 10^{24} \cdot (\tau_{353})^{1/1.3} \quad (1)$$

where the non linear exponent 1/1.3 includes the effect of the dust-growth parameter discussed by Roy et al. (2013) and Okamoto et al. (2017).

Figure 3 shows the correlation between $W(\text{CO})$ and N_{H} derived using Equation (1). We fitted a linear relation to the data points by using the **MPFITEXY** procedure, which provides the slope and intercept by using a χ^2 test (Williams et al. 2010). The slope and intercept were found to be $(3.8 \pm 0.6) \times 10^{20}$ and $(5.7 \pm 0.6) \times 10^{21}$, respectively. The slope corresponds to the molecular component, and the intercept represents the atomic component of the gas Okamoto et al. (2017):

$$N(\text{H}_2) = X(\text{CO}) \cdot W(\text{CO}) \quad (2)$$

$$N_{\text{H}} = 2 \times N(\text{H}_2) + N(\text{HI}) \quad (3)$$

$$N_{\text{H}} = 2X(\text{CO}) \cdot W(\text{CO}) + N(\text{HI}) \quad (4)$$

where $N(\text{HI})$ is the atomic hydrogen column density. We finally obtained $X(\text{CO}) = (1.9 \pm 0.3) \times 10^{20} \text{ cm}^{-2} (\text{K km s}^{-1})^{-1}$ and $N(\text{HI}) = (5.7 \pm 0.6) \times 10^{21} \text{ cm}^{-2}$. We also derived the atomic hydrogen column density $N(\text{HI})'$ by using the Parkes HI data and the following equation (e.g., Dickey & Lockman 1990):

$$N(\text{HI})' = 1.823 \times 10^{18} W(\text{HI}) \quad (5)$$

where $W(\text{HI})$ is the integrated intensity of HI. We obtained $N(\text{HI})' = 5.8 \times 10^{20} \text{ cm}^{-2}$, which is the same as the values of $N(\text{HI})$ obtained from Equations (3) and (4). This finding indicates that the HI surrounding NGC 2359 is optically thin ($\tau \ll 1$). In the present study, we use the value $X(\text{CO}) = 1.9 \times 10^{20} \text{ cm}^{-2} (\text{K km s}^{-1})^{-1}$ and Equation (5) to determine the physical parameters of the molecular and atomic components.

3.3 Molecular and atomic clouds toward NGC 2359

Figure 4 shows the $^{12}\text{CO}(J = 3-2)$ and HI channel maps averaged over 4 km s^{-1} covering the range from 32.2 km s^{-1} to 68.2 km s^{-1} , in which the radio-continuum boundaries are superposed. The HI distribution exhibits bright HI structures at $V_{\text{LSR}} \sim 54$ (Figures 4e–4g) and $\sim 63 \text{ km s}^{-1}$ (Figure 4h), as previously found by Cappa et al. (1999). The component at $V_{\text{LSR}} \sim 54 \text{ km s}^{-1}$ consists of two filamentary HI clouds: one extends from east to southwest (hereafter referred to as the “south HI cloud”), and the other is elongated from north to northwest of the nebula (hereafter referred to as the “north HI cloud”). Both the north and south HI clouds show good spatial correspondence with the radio-shell boundary. In Figure 4h, the southern part of the radio boundary near $(l, b) \sim (227^\circ 85, -0^\circ 12)$ was deformed along with the HI clump at $V_{\text{LSR}} \sim 63 \text{ km s}^{-1}$. These observational trends suggest that both the HI components at $V_{\text{LSR}} \sim 54$ and $\sim 63 \text{ km s}^{-1}$ are likely associated with NGC 2359.

From the CO distribution, we identify three molecular clouds at $V_{\text{LSR}} \sim 37$ (Figures 4a and 4b), ~ 53 (Figures 4d–4g), and $\sim 67 \text{ km s}^{-1}$ (Figure 4i) in the direction of NGC 2359; these values are compatible with previous CO studies (e.g., Schneps et al. 1981; Cappa et al. 2001; Rizzo et al. 2001; Rizzo et al. 2003). The component at $V_{\text{LSR}} \sim 53 \text{ km s}^{-1}$ (hereafter referred to as the “red-shifted CO cloud”) is not only embedded along the radio boundary from east to south but is also correlated with the south HI cloud. The red-shifted CO cloud consists of several tiny clumps with sizes of $\sim 1 \text{ pc}$, and the most intense CO peak is located at $(l, b) \sim (227^\circ 82, -0^\circ 13)$. The component at $V_{\text{LSR}} \sim 37 \text{ km s}^{-1}$ (hereafter referred to as the “blue-shifted CO cloud”) is located at $(l, b) \sim (227^\circ 78, -0^\circ 06)$ along the eastern boundary of the radio shell. In the previous work, the red-shifted CO cloud has been considered associated with the nebula, whereas it has not been clear whether the blue-shifted CO cloud is interacting with the nebula (e.g., Cappa et al. 2001). By contrast, the CO component at $V_{\text{LSR}} \sim 67 \text{ km s}^{-1}$ is located in the southwest region outside of the radio boundary. This finding suggests that the CO cloud at $V_{\text{LSR}} \sim 67 \text{ km s}^{-1}$ appears to be unconnected with NGC 2359. In the present paper, we focus on the blue- and red-shifted CO clouds.

Figure 5 shows the optical image superposed on the CO and HI clouds in the direction of NGC 2359. It is worth noting that the blue- and red-shifted CO clouds appear projected onto the optical dark lane, suggesting that both CO clouds lie inside or in front of the nebula. We also find that the spatial distribution of the blue-shifted CO cloud is complementary to that of the red-shifted CO cloud. Furthermore, both the south and north HI clouds nicely trace not only the boundary of the radio shell but also the boundary of the optical filaments. In particular, the south HI cloud is located along the red-shifted CO cloud up to the boundary of the blue-shifted CO cloud.

To estimate the mass M of the CO cloud, we used the following equation:

$$M = \mu m_{\text{H}} \Omega d^2 \sum_i N_i(\text{H}_2), \quad (6)$$

where $\mu = 2.8$ is mean molecular weight, taking into account a helium abundance of 20%, m_{H} is the mass of the hydrogen atom, Ω is the solid angle of a square pixel, d is the distance to the molecular cloud, and $N_i(\text{H}_2)$ is the molecular hydrogen column density for each pixel. Both the blue- and red-shifted CO clouds have masses of $\sim 700 M_{\odot}$ to $800 M_{\odot}$ at the distance of 5 kpc, consistent with the study of Cappa et al. (2001). The maximum values of $N(\text{H}_2)$ for the blue-shifted CO cloud is found to be $\sim 3.6 \times 10^{21} \text{ cm}^{-2}$, whereas that of the red-shifted CO cloud is $\sim 5.1 \times 10^{21} \text{ cm}^{-2}$. The mass and column density of the HI clouds also are roughly consistent with previous work (Cappa et al. 1999). We summarize the physical properties of the CO and HI clouds in Table 1. We note that the velocity width of the red-shifted CO cloud is larger than that of the blue-shifted CO cloud, thus suggesting that the degrees of heating/ionization due to the WR star are different for the two CO clouds.

3.4 Physical conditions in the CO clouds

To investigate the physical conditions in the blue- and red-shifted CO clouds, we determined that spatial distributions of the intensity ratio $R_{3-2/1-0}$ for CO $J = 3-2 / 1-0$ by using the ASTE and Nobeyama 45 m CO data. Figure 6 shows the $R_{3-2/1-0}$ distributions for the CO clouds. In the blue-shifted CO cloud (Figure 6a), the highest value, $R_{3-2/1-0} > 0.6$, is seen in the northeastern part, which is on the far side from the center of the nebula, whereas other regions show low values, $R_{3-2/1-0} < 0.3$. In the red-shifted CO cloud (Figure 6b), we see a high intensity ratio, $R_{3-2/1-0} > 1.0$, from the entire region, which nicely traces the optical nebula. Figure 7 shows typical CO spectra at six positions in the blue-shifted CO cloud (B1 and B2) and the red-shifted CO cloud (R1–R4) (see also Table 1). We estimate that values of $R_{3-2/1-0}$ is ~ 0.7 for B1, ~ 0.3 for B2, ~ 0.9 – 1.0 for R1–R3, and ~ 0.6 for R4.

To investigate the origin of the highly excited gas in both the blue- and red-shifted CO clouds, we performed a Large Velocity Gradient analysis (LVG; e.g., Goldreich & Kwan 1974). To determine the relation between the number density of molecular hydrogen $n(\text{H}_2)$ and the kinematic temperature T_{k} of the CO clouds as functions of $R_{3-2/1-0}$, we assumed $X/(dv/dr) \sim 2 \times 10^{-5}$ for the blue-shifted CO cloud and $\sim 1 \times 10^{-4}$ for the red-shifted CO cloud, where X is the abundance ratio of $^{12}\text{CO}/\text{H}_2$ ($= 1 \times 10^{-4}$; c.f., Frerking et al. 1982), and dv/dr is the velocity gradient of the CO clouds. We adopt $dv/dr \sim 0.2 \text{ km s}^{-1} \text{ pc}^{-1}$ for the blue-shifted CO cloud and $\sim 1.0 \text{ km s}^{-1} \text{ pc}^{-1}$ for the red-shifted CO cloud.

Figure 8a shows the LVG result for the blue-shifted CO cloud. To determine the number

density of molecular hydrogen $n(\text{H}_2)$ at the positions B1 and B2, we first derived the excitation temperature T_{ex} , assuming the local thermodynamic equilibrium (LTE):

$$T_{\text{ex}} = 5.53 / \ln\{1 + 5.53 / (T_{\text{peak}}^{12\text{CO}(J=1-0)} + 0.819)\}, \quad (7)$$

where $T_{\text{peak}}^{12\text{CO}(J=1-0)}$ is the peak brightness temperature of the $^{12}\text{CO}(J = 1-0)$ line emission. The quantities $T_{\text{peak}}^{12\text{CO}(J=1-0)}$ and T_{ex} were found to be ~ 13 and ~ 16 K, respectively. Given that $T_{\text{ex}} = T_{\text{k}}$ in LTE, we found $n(\text{H}_2)$ for B1 ($R_{3-2/1-0} \sim 0.7$) and B2 ($R_{3-2/1-0} \sim 0.3$) to be ~ 2000 and ~ 400 cm^{-3} , respectively. By contrast, we constrain the kinematic temperature T_{k} of the red-shifted CO cloud by using the LVG result shown in Figure 8b. Considering that a typical value of $R_{3-2/1-0}$ is 0.9–1.0 for the red-shifted CO cloud (see also Figure 6), the value of T_{k} is at least ~ 40 K, thus indicating that the temperature of the red-shifted CO cloud has been increased because of heating by the WR star.

3.5 Position–velocity diagrams for CO and HI

Figure 9 shows the velocity–galactic longitude diagram for HI and CO. The blue- and red-shifted CO clouds have a peak velocity separation of ~ 17 km s^{-1} (see also Table 1). We note that the red-shifted CO cloud shows elongated velocity structures extending to $V_{\text{LSR}} \sim 44$ km s^{-1} , which are roughly consistent with the $^{12}\text{CO}(J = 2-1)$ results presented by Rizzo et al. (2003). Interestingly, the bridging features extended in the direction of the blue-shifted CO cloud but not in the same direction of the WR star (shown as the dashed line). We also find diffuse HI components at $V_{\text{LSR}} \sim 41$ km s^{-1} , which appear to connect the blue- and red-shifted CO clouds.

4 Discussion

4.1 Isolated WR star formation triggered by a cloud–cloud collision

According to Fukui et al. (2017b), the observational signatures of high-mass star formation triggered by cloud–cloud collisions are generally categorized by three elements: (1) the two colliding clouds generally show a supersonic velocity separation in the range ~ 10 km s^{-1} to 30 km s^{-1} ; (2) a bridging feature connects the two clouds in velocity space; (3) the spatial distributions of the two clouds are complementary to each other. In this section, we demonstrate that NGC 2359 satisfies all three observational signatures, thus making the cloud–cloud collision scenario entirely reasonable as the mechanism that formed the isolated WR star in NGC 2359.

In NGC 2359, the velocity separation of the blue- and red-shifted CO clouds is ~ 16 km s^{-1} in the direction of the line-of-sight (hereafter referred to as the l.o.s.). Table 2 summarizes the physical

parameters of molecular clouds toward isolated O-type stars formed by cloud-cloud collisions. The large velocity separation in NGC 2359 is similar to that in the HII region RCW 120 (Torii et al. 2015). We argue that these large velocity separations cannot be created by stellar feedback from the high-mass star. In the case of NGC 2359, the total momentum of the neutral interstellar gas is $\sim 2 \times 10^4 M_{\odot} \text{ km s}^{-1}$, assuming that the velocity of the expanding gas is half the value of the velocity separation $\sim 8 \text{ km s}^{-1}$ of the two clouds. On the contrary, the momentum typically available from the stellar wind from a WR star is $\sim 2.3 \times 10^4 M_{\odot} \text{ km s}^{-1}$ (Abbott 1982). Therefore, the required momentum is at least $\sim 90\%$ of that available from the stellar wind, which exceeds the theoretical maximum of $\sim 20\%$ that can be transferred from wind (e.g., Weaver et al. 1977). Furthermore, the small solid angle subtended by the molecular/atomic clouds reduces the effective momentum transfer to the clouds.

In Figure 9, the elongated velocity structure of the red-shifted CO cloud can be interpreted as part of a bridging feature connecting the red- and blue-shifted CO clouds. According to numerical simulations of cloud-cloud collisions, turbulent gas motions in the shock-compressed layer can be observed in a position-velocity diagram as an intermediate velocity component connecting two colliding clouds (e.g., Takahira et al. 2014; Haworth et al. 2015a; Haworth et al. 2015b). Furthermore, the HI feature at $V_{\text{LSR}} \sim 41 \text{ km s}^{-1}$ may also be understood as a bridging feature, similar to the case of the HII region RCW 120. Torii et al. (2015) argue that the interstellar molecular/atomic gases associated with RCW 120 exhibit no expanding motions; hence, the elongated and intermediate velocity structures observed in that HII region were formed by a cloud-cloud collision. By contrast, Rizzo et al. (2003) claim that the elongated velocity structure of CO in NGC 2359 can be separated into three different velocity components that they suggest were formed by several energetic events during the earlier luminous-blue-variable phase and/or the actual WR stage of HD 56925. Moreover, Rizzo et al. (2003) found a large HI shell with a size of $70 \text{ pc} \times 37 \text{ pc}$ in the direction of NGC 2359; this shell shows an expanding motion of $\sim 12 \text{ km s}^{-1}$. However, given the coarse angular resolution of the CO and HI observations, no conclusive evidence exists that the CO multiple-velocity layers and the HI expanding motions are physically connected with any past activity of HD 56925. Further CO and HI observations with a fine angular resolution using the Atacama Large Millimeter/submillimeter Array (ALMA), VLA, and Australia Telescope Compact Array interferometers are needed to clarify the detailed kinematics of the neutral interstellar gas associated with NGC 2359.

The spatial distribution of the blue-shifted CO cloud is complementary to that of the red-shifted CO cloud or HI cloud (see Figure 5); this distribution is a typical signature of a collision between a small and large cloud (e.g., Habe & Ohta 1992; Anathpindika 2010; Takahira et al. 2014, 2017). Furthermore, the bent shape of the red-shifted CO cloud is similar to the case of the dense dust

core AGAL G337.916–00.477. According to Torii et al. (2017d, 2017e), the infrared bent shape in AGAL G337.916–00.477 was formed either by the expansion of the HII region or by a cloud-cloud collision. In the latter case, the small colliding cloud has the potential to bend the large cloud through strong compression at the shocked layer (Torii et al. 2017e). Given that NGC 2359 satisfies all the observational signatures of a cloud-cloud collision, we conclude that NGC 2359 and the isolated WR star HD 56925 were likely created by a cloud-cloud collision.

4.2 Evolutionary stage and collisional time scale

We claim that the evolutionary stage of NGC 2359 corresponds to the final phase of a cloud-cloud collision. Figure 10 shows a schematic illustration of the cloud-cloud collision model presented by Habe & Ohta (1992) and by Torii et al. (2015), with minor updates. First, a small cloud collides with a large cloud at a supersonic velocity (stage 0). Subsequently, the small colliding cloud creates a shock-compressed layer (stage I), which forms an O-type star in the dense gas clump (stage II). If the velocity of the colliding cloud remains high, the shock-compressed layer continues to burrow into the large cloud (stage III) and, finally, to penetrate it (stage IV). In stage IV, the O-type star can be observed as a WR star with a wind-blown bubble, which is agreement with the case of NGC 2359.

Figure 11a shows an illustration of the cloud-cloud collision in NGC 2359 presented in the galactic longitude–latitude plane. It is likely that the blue-shifted CO cloud collided with the red-shifted CO and HI clouds from west and that the blue-shifted CO cloud contained a larger amount of gas before the collision than after the collision. The collision then created an isolated O-type star in the shock-compressed layer, which has been moved in the figure to the position of the observed blue-shifted CO cloud. The O-type star illuminates the cavity in the large cloud formed by the collision, finally, transforming it into a WR star with a wind-blown bubble.

This interpretation is also compatible with numerical simulations using smoothed particle hydrodynamics codes. According to Anathpindika (2010), a collision between a small and a large cloud forms a V-shaped gas structure pointing in the direction of the collision (similar to stage IV in Figure 10). Furthermore, the author found that the small penetrating cloud shows a density gradient along the collisional direction (see Figure 1 of Anathpindika 2010). In NGC 2359, the red-shifted CO and HI clouds show similar V-shaped structures west of the nebula. Moreover, the eastern part of the blue-shifted CO cloud, which corresponds to the direction of collision, shows a density that is five times higher than the western (see Section 3.4). Therefore, we conclude that the blue-shifted CO cloud likely collided from the west and has penetrated through the nebula.

The collision time scale is important for understanding the cloud-cloud collision in NGC 2359.

It is thought that a WR star is formed after passing through the main-sequence phase of an O-type star, the typical lifetime of which is ~ 1.5 Myr or longer (e.g., Meynet & Maeder 2005). For consistency with this time scale, the blue-shifted CO cloud must have collided with at a collision angle of 70° or higher relative to the l.o.s. Figure 11b shows a schematic illustration of the cloud-cloud collision in NGC 2359 presented in the galactic longitude–l.o.s. plane. The distance between the WR star and the blue-shifted CO cloud is ~ 26 pc, and the collision velocity is ~ 17 km s $^{-1}$, assuming a collision angle of 70° . With these parameters, the collision timescale is ~ 1.5 Myr. Furthermore, the large distance between the WR star and the blue-shifted CO cloud is also consistent with the low kinematic temperature ~ 16 K in the blue-shifted CO cloud; it is too distant to be strongly affected by heating from the WR star.

4.3 Comparison with other isolated O-type stars formed by cloud-cloud collisions

We argue that there is no significant difference between the physical properties of the colliding clouds that produce isolated O-type stars and those that of WR stars. As mentioned in Section 4.1, NGC 2359 exhibits physical properties similar to those of RCW 120 with regard to the velocity separation, bridging features, and complementary spatial distributions between the two colliding clouds. On the contrary, the values of the mass and column density of NGC 2359 are the lowest in Table 2. We argue that this result is an insignificant difference, particularly because ionized material cannot be traced by CO and HI emission lines. According to Cappa et al. (1999), the total mass of ionized matter associated with NGC 2359 is ~ 850 – $1100 M_\odot$ according to radio-continuum observations from the VLA. Therefore, the total mass of neutral and ionized gas in NGC 2359 is at least ~ 2.6 – $2.8 \times 10^3 M_\odot$, similar to the value for M20, which has a total molecular mass of $\sim 2 \times 10^3 M_\odot$. Moreover, the observed mass and column density of NGC 2359 are lower limits, because some of the CO molecules are expected to be photo-dissociated by the strong UV radiation from the WR star, particularly in the red-shifted CO cloud. Further observations of neutral and ionized carbon by using ALMA and SOFIA are needed to determine accurately the total amount of interstellar gas and the degree of ionization of the interstellar gas toward NGC 2359.

Accurate measurements of the interstellar gas also are important for determining the key physical properties (mass, column density, relative velocity separation, etc.) that are necessary to obtain the spectral types of high-mass stars formed by cloud-cloud collisions. In Table 2, we find a weak trend that column densities increase as O-type stars become early spectral types, except for the case of NGC 2359. To investigate this interesting relation, we need to have a large sample of cloud-cloud collisions in the directions of isolated O-type and WR stars.

5 Conclusions

We have made new $^{12}\text{CO}(J = 1-0, 3-2)$ observations of the WR nebula NGC 2359 by using the Nobeyama 45-m and ASTE radio telescopes. By using these results, we have shown that the WR star HD 56925 in NGC 2359 was likely to have been formed by a cloud-cloud collision. We summarize the main results obtained in this study below:

1. We have determined the large-scale distributions of interstellar neutral molecular and atomic hydrogen and have compared them with the distributions of dust opacity and temperature. Following the method described by Okamoto et al. (2017), we have obtained the result of $X(\text{CO}) = 1.9 \times 10^{20} \text{ cm}^{-2} (\text{K km s}^{-1})^{-1}$ for the conversion factor between the integrated CO intensity and the molecular hydrogen column density. We have also found that the neutral hydrogen around NGC 2359 is optically thin.
2. A new analysis of CO and HI has revealed that two molecular clouds and two atomic clouds are likely associated with NGC 2359. The blue-shifted CO cloud (at $V_{\text{LSR}} = 35.8\text{--}37.8 \text{ km s}^{-1}$) and the red-shifted CO cloud (at $V_{\text{LSR}} = 42.6\text{--}57.0 \text{ km s}^{-1}$) appear projected onto an optical dark lane, thus suggesting that both CO clouds lie either inside or in front of the nebula. The two atomic clouds, namely, the north and south HI clouds (at $V_{\text{LSR}} = 48.2\text{--}63.0 \text{ km s}^{-1}$), not only trace nicely the boundary of the radio continuum shell but also trace the optical filaments. In particular, the south HI cloud is located along the red-shifted CO cloud up to the boundary of the blue-shifted CO cloud. The masses of the blue- and red-shifted CO clouds and the HI cloud are determined to be ~ 800 , ~ 700 , and $\sim 230 M_{\odot}$, respectively.
3. On the basis of an LVG analysis using the intensity ratio of CO $J = 3-2/1-0$, we find the kinematic temperature of the red-shifted CO cloud to be at least $\sim 40 \text{ K}$, thus indicating that the cloud temperature has been increased because of the heating by the WR star. By contrast, the blue-shifted CO cloud shows a low kinematic temperature of $\sim 16 \text{ K}$ under the LTE assumption. We have also found that the eastern part of the blue-shifted cloud has a density five times higher than the western part.
4. NGC 2359 and the isolated WR star HD 56925 were possibly created by a collision between the blue- and red-shifted CO clouds. The supersonic velocity separation of the two clouds cannot be caused by stellar feedback from the WR star. Furthermore, the complementary spatial distributions and bridging features of CO and HI are in good agreement with the expected observational signatures of high-mass star formation triggered by cloud-cloud collisions (e.g., Fukui et al. 2017b). We argue that the evolutionary stage of NGC 2359 corresponds to the last phase of a cloud-cloud collision with a collision timescale $\sim 1.5 \text{ Myr}$ or longer. We have also noted that there is no signif-

icant difference between the physical properties of the colliding clouds that trigger the formation of isolated O-type stars and WR stars.

Acknowledgments

The authors would like to thank Robert Franke from the Focal Pointe Observatory for providing the optical images of NGC 2359. The NANTEN project is based on a mutual agreement between Nagoya University and the Carnegie Institution of Washington (CIW). We appreciate the hospitality of all the staff members of the Las Campanas Observatory of CIW. We are thankful to many Japanese companies and public donors who contributed to the realization of the project. The ASTE telescope is operated by National Astronomical Observatory of Japan (NAOJ). The Nobeyama 45-m radio telescope is operated by Nobeyama Radio Observatory, a branch of NAOJ. This work was financially supported by Grants-in-Aid for Scientific Research (KAKENHI) of the Japanese society for the Promotion of Science (JSPS, grant No. 15H05694). This work also was supported by “Building of Consortia for the Development of Human Resources in Science and Technology” of Ministry of Education, Culture, Sports, Science and Technology (MEXT, grant No. 01-M1-0305). We acknowledge to Kosuke Fujii and Hiroaki Iwamura for contributions on the observations of $^{12}\text{CO}(J = 3-2)$ and $^{12}\text{CO}(J = 1-0)$ data.

References

- Abbott, D. C. 1982, *ApJ*, 263, 723
- Anathpindika, S. V. 2010, *MNRAS*, 405, 1431
- Cappa, C. E., Goss, W. M., Niemela, V. S., & Ostrov, P. G. 1999, *AJ*, 118, 948
- Cappa, C. E., Rubio, M., & Goss, W. M. 2001, *AJ*, 121, 2664
- Crampton, D. 1971, *MNRAS*, 153, 303
- Crowther, P. A. 2007, *ARA&A*, 45, 177
- Dewangan, L. K. 2017, *ApJ*, 837, 44
- Dickey, J. M., & Lockman, F. J. 1990, *ARA&A*, 28, 215
- Ezawa, H., Kawabe, R., Kohno, K., & Yamamoto, S. 2004, *Proc. SPIE*, 5489, 763
- Fich, M., & Blitz, L. 1984, *ApJ*, 279, 125
- Frerking, M. A., Langer, W. D., & Wilson, R. W. 1982, *ApJ*, 262, 590
- Fujita, K., et al. 2017, in preparation
- Fukui, Y., Ohama, A., Hanaoka, N., et al. 2014, *ApJ*, 780, 36
- Fukui, Y., Harada, R., Tokuda, K., et al. 2015, *ApJL*, 807, L4
- Fukui, Y., Torii, K., Ohama, A., et al. 2016, *ApJ*, 820, 26
- Fukui, Y., Tsuge, K., Sano, H., et al. 2017a, *PASJ*, 69, L5
- Fukui, Y., Torii, K., Hattori, Y., et al. 2017b, arXiv:1701.04669
- Fukui, Y., Kohno, M., Yokoyama, K., et al. 2017c, arXiv:1706.05768
- Fukui, Y., Kohno, M., Yokoyama, K., et al. 2017d, arXiv:1706.05771

Fukui, Y., Hattori, Y., Torii, K., et al. 2017e, arXiv:1706.08720

Furukawa, N., Dawson, J. R., Ohama, A., et al. 2009, ApJL, 696, L115

Georgelin, Y. M., Georgelin, Y. P., & Roux, S. 1973, A&A, 25, 337

Goldreich, P., & Kwan, J. 1974, ApJ, 189, 441

Goudis, C., Hippelein, H., & Muench, G. 1983, A&A, 117, 127

Goudis, C. D., Christopoulou, P.-E., Meaburn, J., & Dyson, J. E. 1994, A&A, 285, 631

Habe, A., & Ohta, K. 1992, PASJ, 44, 203

Hasegawa, T., Sato, F., Whiteoak, J. B., & Miyawaki, R. 1994, ApJL, 429, L77

Haworth, T. J., Tasker, E. J., Fukui, Y., et al. 2015a, MNRAS, 450, 10

Haworth, T. J., Shima, K., Tasker, E. J., et al. 2015b, MNRAS, 454, 1634

Hayashi, K., Sano, H., Enokiya, R., et al. 2017, arXiv:1706.05871

Inoue, T., & Fukui, Y. 2013, ApJL, 774, L31

Inoue, T., Hennebelle, P., Fukui, Y., et al. 2017, arXiv:1707.02035

Kalberla, P. M. W., & Haud, U. 2015, A&A, 578, A78

Kamazaki, T., Okumura, S. K., Chikada, Y., et al. 2012, PASJ, 64, 29

Kohno, M., Torii, K., Tachihara, K., et al. 2017, arXiv:1706.07964

Kuno, N., Takano, S., Iono D., et al. 2011, General Assembly and Scientific Symposium, 2011 XXXth URSI,
1

Lozinskaya, T. A. 1973, Soviet Ast., 17, 317

Martins, F., Pomarès, M., Deharveng, L., Zavagno, A., & Bouret, J. C. 2010, A&A, 510, A32

McLean, B. J., Greene, G. R., Lattanzi, M. G., & Pirenne, B. 2000, Astronomical Data Analysis Software and
Systems IX, 216, 145

Meaburn, J., Dyson, J. E., Goudis, C. D., & Christopoulou, P. E. 1994, Ap&SS, 216, 281

Meynet, G., & Maeder, A. 2005, A&A, 429, 581

Mizuno, A., & Fukui, Y. 2004, Milky Way Surveys: The Structure and Evolution of our Galaxy, 317, 59

Nakajima, T., Kimura, K., Nishimura, A., et al. 2013, PASP, 125, 252

Nishimura, A., Costes, J., Inaba, T., et al. 2017a, arXiv:1706.06002

Nishimura, A., Minamidani, T., Umemoto, T., et al. 2017b, arXiv:1706.06956

Okamoto, R., Yamamoto, H., Tachihara, K., et al. 2017, ApJ, 838, 132

Okawa, K., et al. 2017, in preparation

Ohama, A., Dawson, J. R., Furukawa, N., et al. 2010, ApJ, 709, 975

Ohama, A., Kono, M., Tsutsumi, D., et al. 2017, arXiv:1706.05659

Peimbert, M., Rayo, J. F., & Torres-Peimbert, S. 1978, ApJ, 220, 516

Planck Collaboration, Abergel, A., Ade, P. A. R., et al. 2014, A&A, 571, A11

Rizzo, J. R., Martín-Pintado, J., & Mangum, J. G. 2001, *A&A*, 366, 146
Rizzo, J. R., Martín-Pintado, J., & Desmurs, J.-F. 2003, *A&A*, 411, 465
Roy, A., Martin, P. G., Polychroni, D., et al. 2013, *ApJ*, 763, 55
Saigo, K., Onishi, T., Nayak, O., et al. 2017, *ApJ*, 835, 108
Sano, H., Enokiya, R., Hayashi, K., et al. 2017, arXiv:1706.05763
Sawada, T., Ikeda, N., Sunada, K., et al. 2008, *PASJ*, 60, 445
Schneps, M. H., Haschick, A. D., Wright, E. L., & Barrett, A. H. 1981, *ApJ*, 243, 184
Smith, L. F. 1968, *MNRAS*, 141, 317
Smith, L. F., Shara, M. M., & Moffat, A. F. J. 1996, *MNRAS*, 281, 163
Sorai, K., Sunada, K., Okumura, S. K., et al. 2000, *Proc. SPIE*, 4015, 86
Takahira, K., Tasker, E. J., & Habe, A. 2014, *ApJ*, 792, 63
Takahira, K., Shima, K., Tasker, E. J., & Habe, A. 2017, arXiv:1706.08656
Talent, D. L., & Dufour, R. J. 1979, *ApJ*, 233, 888
Torii, K., Enokiya, R., Sano, H., et al. 2011, *ApJ*, 738, 46
Torii, K., Hasegawa, K., Hattori, Y., et al. 2015, *ApJ*, 806, 7
Torii, K., Hattori, Y., Hasegawa, K., et al. 2017a, *ApJ*, 835, 142
Torii, K., Hattori, Y., Matsuo, M., et al. 2017b, arXiv:1706.07164
Torii, K., Matsuo, M., Fujita, S., et al. 2017c, submitted to *PASJ*
Torii, K., Hattori, Y., Hasegawa, K., et al. 2017d, *ApJ*, 840, 111
Torii, K., et al. 2017e, in preparation
Treffers, R. R., & Chu, Y.-H. 1982, *ApJ*, 254, 569
Tsuboi, M., Miyazaki, A., & Uehara, K. 2015, *PASJ*, 67, 109
Tsuge, K., et al. 2017, in preparation
van der Hucht, K. A., Conti, P. S., Lundstrom, I., & Stenholm, B. 1981, *Space Sci. Rev.*, 28, 227
van der Hucht, K. A. 2001, *New A Rev.*, 45, 135
Voisin, F., Rowell, G., Burton, M. G., et al. 2016, *MNRAS*, 458, 2813
Wang, Y., Jaffe, D. T., Graf, U. U., & Evans, N. J., II 1994, *ApJS*, 95, 503
Weaver, R., McCray, R., Castor, J., Shapiro, P., & Moore, R. 1977, *ApJ*, 218, 377
Williams, M. J., Bureau, M., & Cappellari, M. 2010, *MNRAS*, 409, 1330
Wolfire, M. G., & Cassinelli, J. P. 1987, *ApJ*, 319, 850

Table 1. Physical Properties of CO and HI Clouds associated with NGC 2359

Cloud Name	l	b	T_R^*	V_{peak}	ΔV_{LSR}	Size	Column Density	Mass	Comment
	(degree)	(degree)	(K)	(km s ⁻¹)	(km s ⁻¹)	(pc)	($\times 10^{21}$ cm ⁻²)	(M_{\odot})	
(1)	(2)	(3)	(4)	(5)	(6)	(7)	(8)	(9)	(10)
Blue-shifted CO cloud	227.78	-0.04	3.7	36.7	1.0	5.1	3.6	800	B1
	227.78	-0.08	2.7	36.9	1.1				B2
Red-shifted CO cloud	227.80	-0.07	2.0	53.1	2.2	3.6	7.9	700	R1
	227.80	-0.13	3.1	53.5	3.9				R2
	227.82	-0.13	8.7	53.3	4.3				R3
	227.81	-0.16	4.3	52.6	3.7				R4
North HI cloud	227.69	-0.11	14.8 / 13.3	52.8 / 63.3	4.3 / 3.2	7.8	0.2	30	
South HI cloud	227.81	-0.16	22.3 / 13.3	55.4 / 64.2	6.2 / 2.4	16.9	0.4	200	
	227.84	-0.23	19.0	54.1	7.1				

Note. — Col. (1): Cloud name. Cols. (2–3) Position of the maximum $^{12}\text{CO}(J=3-2)$ and HI intensities for each component. Cols. (4–6) Physical properties of the $^{12}\text{CO}(J=3-2)$ and HI emission lines obtained at each position. Col. (4): Peak radiation temperature, T_R^* . Col. (5): V_{peak} derived from a Gaussian fitting. Col. (6): line width of Full-width half-maximum (FWHM), ΔV_{LSR} . Col. (7): CO/HI cloud size defined as $(A/\pi)^{0.5} \times 2$, where A is the total cloud surface area surrounded by the 5σ level in the integrated intensities of the CO/HI cloud. Col. (8): Regarding the CO clouds, the molecular hydrogen column density $N_{\text{H}}(\text{H}_2)$ derived from the $^{12}\text{CO}(J=1-0)$ integrated intensity, $W(^{12}\text{CO})$, $N(\text{H}_2) = 1.9 \times 10^{20} [W(^{12}\text{CO})/(\text{K km s}^{-1})]$ (cm⁻²) (see in the text). Regarding the HI clouds, the atomic hydrogen column density $N_{\text{H}}(\text{HI})$ derived using the equations of $N_{\text{H}}(\text{HI}) = 1.823 \times 10^{18} W(\text{HI})$. Col. (9): Mass of the cloud derived using the relation between the molecular or atomic hydrogen column density, shown in Col. (8).

Table 2. Physical properties of molecular clouds toward the isolated O-type stars formed by cloud-cloud collisions

Name	Molecular mass	$N(\text{H}_2)$	Relative velocity	Complementary distribution	Bridging feature	Age	Number of O-type stars	Spectral type	References
(1)	$[M_\odot]$	$[\text{cm}^{-2}]$	$[\text{km s}^{-1}]$	(5)	(6)	[Myr]	(8)	(9)	(10)
M20	1×10^3	1×10^{22}	7.5	yes	yes	~ 0.3	1	O7.5V	[1, 2]
	1×10^3	1×10^{22}							
RCW 120	5×10^4	3×10^{22}	20	yes	yes	~ 0.2 < 5.0	1	O6–8V	[3] [4]
	4×10^3	8×10^{21}							
N159W-South	9×10^3	1×10^{23}	8^\dagger	no	no	~ 0.06	1	—	[5]
	6×10^3	1×10^{23}							
N159E-Papillon	5×10^3	4×10^{22}	9^\dagger	no	no	~ 0.2	1	$> \text{O3}$	[6]
	7×10^3	4×10^{22}							
	8×10^3	6×10^{22}							
RCW 34	3×10^4	2×10^{22}	5	yes	yes	~ 0.2	1	O8.5V	[7]
	1×10^3	2×10^{21}							
NGC 2359	8×10^2	4×10^{21}	16	yes	yes	> 1.5	1	WN4	This work
	7×10^2	8×10^{21}							

Note. — Col. (1): HII region name. Cols. (2–3) Physical properties of collided two or three clouds. Col. (2) Molecular mass. Col. (3) Molecular column density $N(\text{H}_2)$. Cols. (4–6) Relation among the two or three clouds. Col. (4) Relative velocity separation. Col. (5) Complementary spatial distribution. Col. (6) Bridging feature in the velocity space. Col. (7) Age of the cluster or O-type star. Col. (8) Number of O-type stars. Col. (9) Cluster type. SSC and SC indicate Super Star Cluster and Star Cluster. Col. (10) References. [1] Torii et al. 2011, [2] Torii et al. 2017a, [3] Martins et al. 2010, [4] Torii et al. 2015, [5] Fukui et al. 2015, [6] Saigo et al. 2017, [7] Hayashi et al. 2017.

† Corrected for the projection effect.

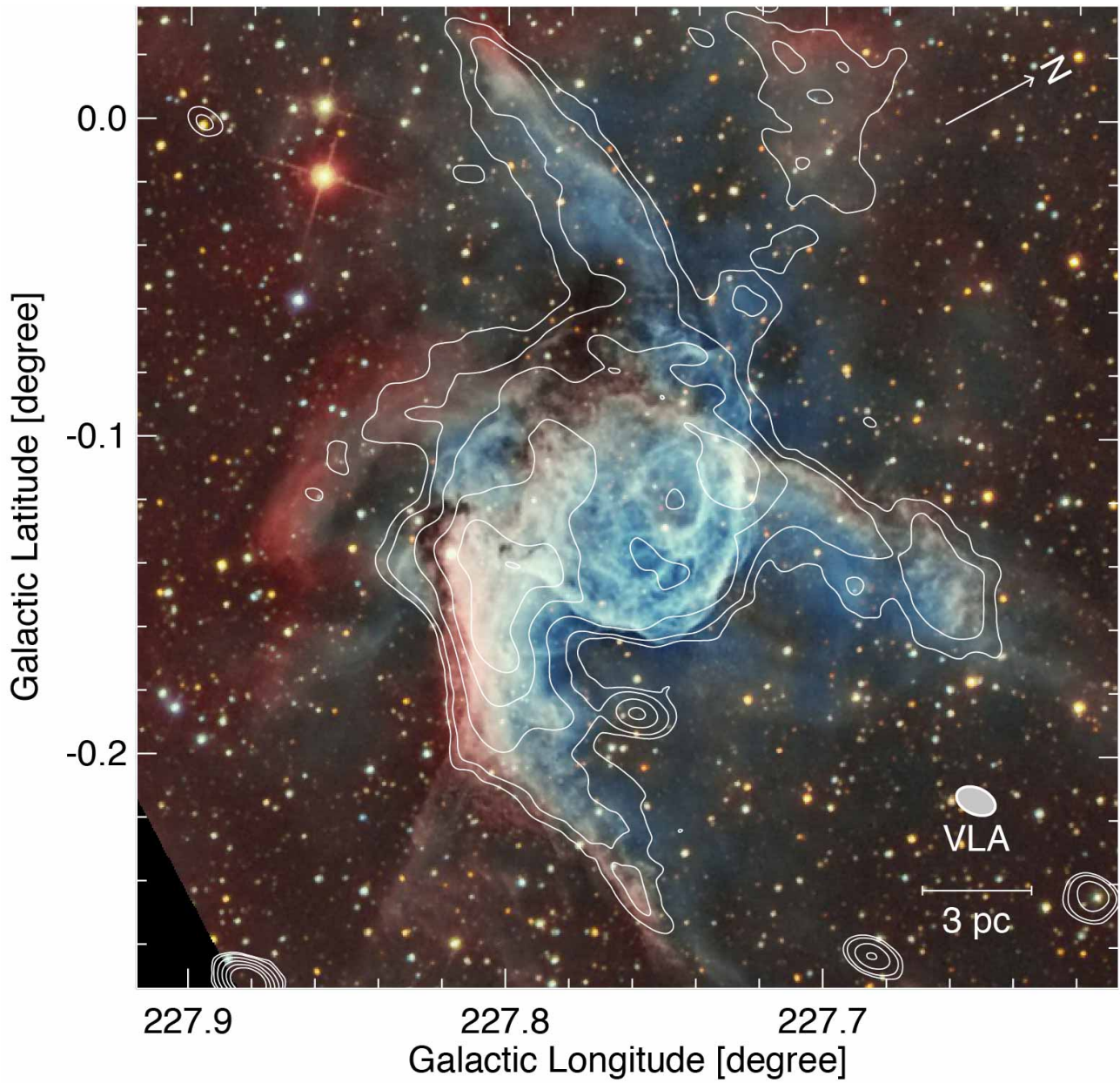


Fig. 1. Optical image of the Wolf-Rayet nebula NGC 2359 (courtesy of Robert Franke) obtained at the Focal Pointe Observatory. The red and green/blue represent H α and OIII emissions, respectively. Superposed contours indicate the radio continuum with VLA (Cappa et al. 1999). The contour levels are 1.5, 2.2, 4.3, 7.8, 12.7, and 19.0 K.

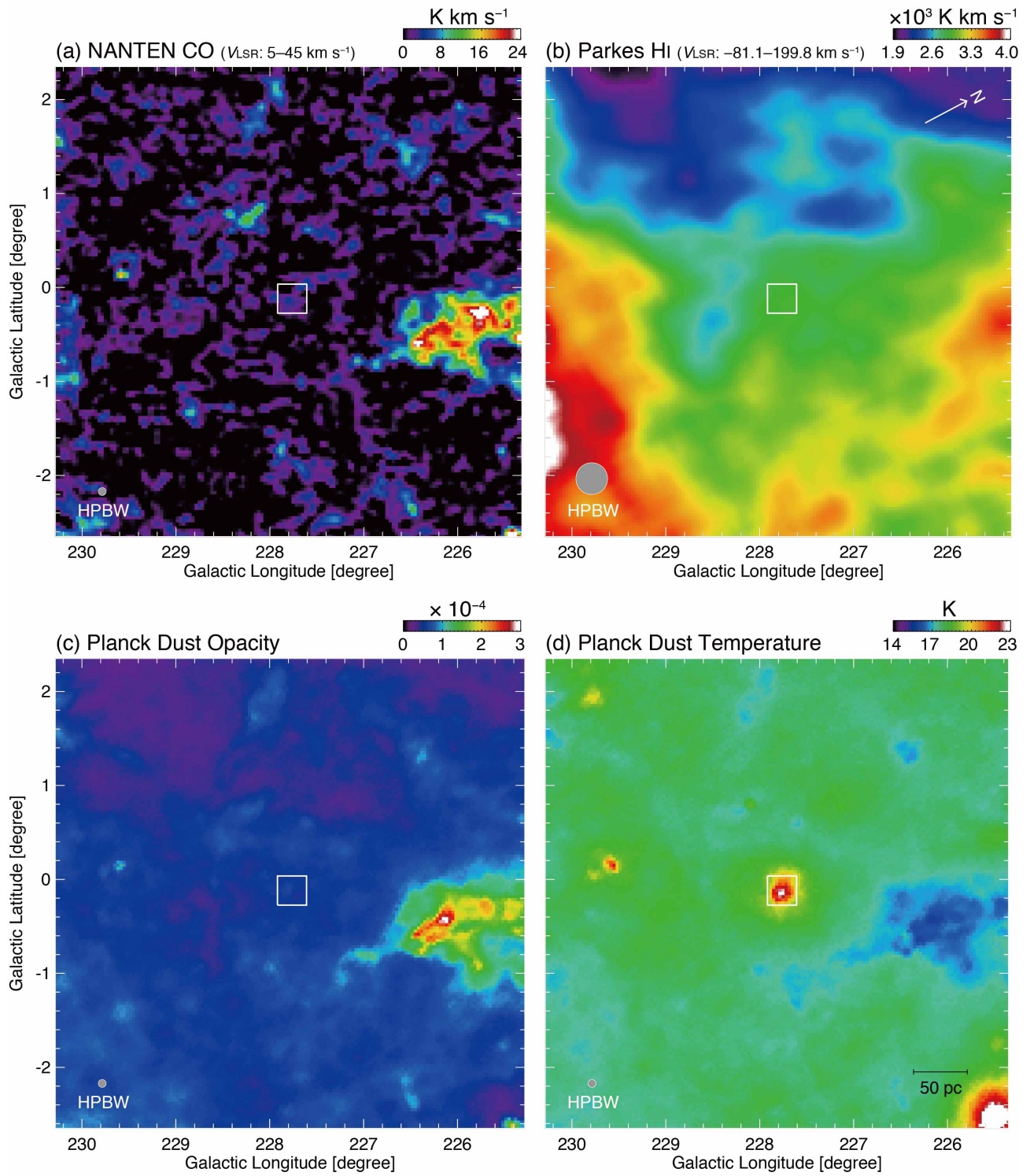


Fig. 2. Maps of (a) NANTEN $^{12}\text{CO } J=1\text{--}0$, (b) *Planck* dust opacity of 353 GHz, and (c) *Planck* dust temperature toward NGC 2359. Size of each map is 5 degree \times 5 degree.

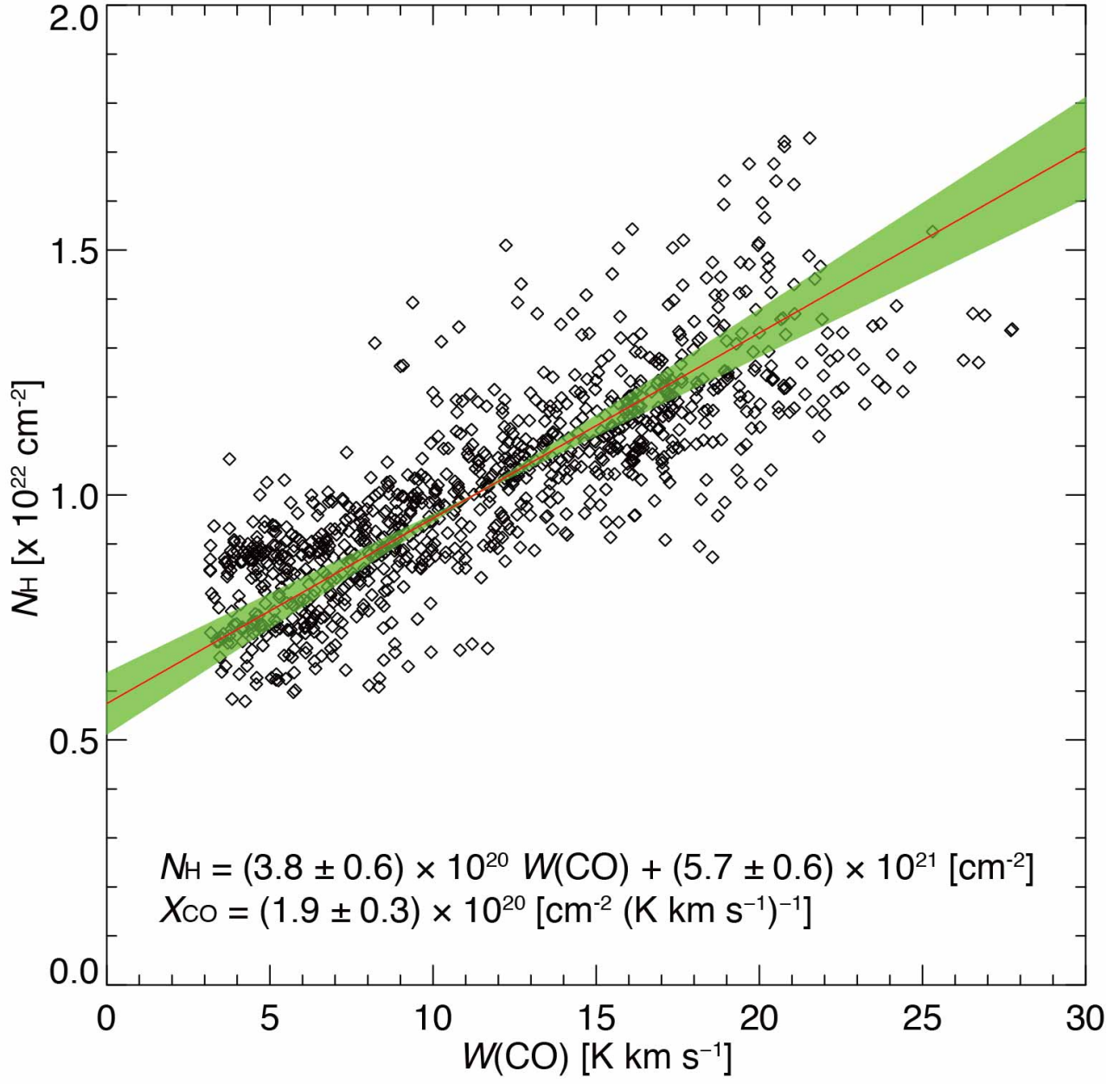


Fig. 3. Correlation plot between the integrated CO intensity $W(\text{CO})$ and the total proton column density N_H .

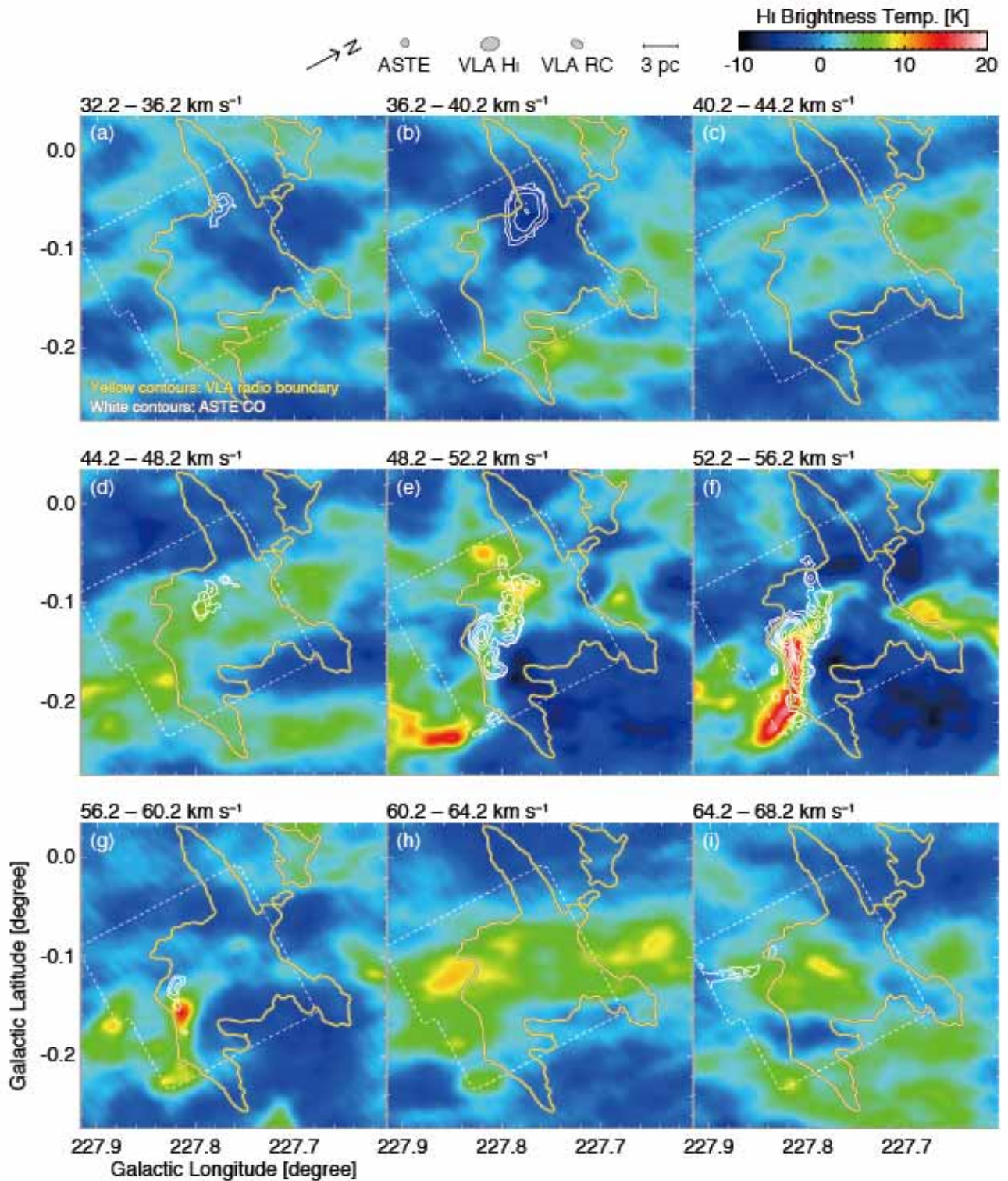


Fig. 4. Velocity channel maps of H I (*color image*) and $^{12}\text{CO}(J = 3-2)$ brightness temperature (*white contours*). Superposed yellow contours indicate the radio continuum boundary of 1.5 K. Each panel of CO/H I shows intensity distributions averaged every 4.0 km s^{-1} in a velocity range from 32.2 to 68.2 km s^{-1} following the color-bar shown on the upper right. The contour levels of CO are from 3, 4, 5, 6, and 7 K.

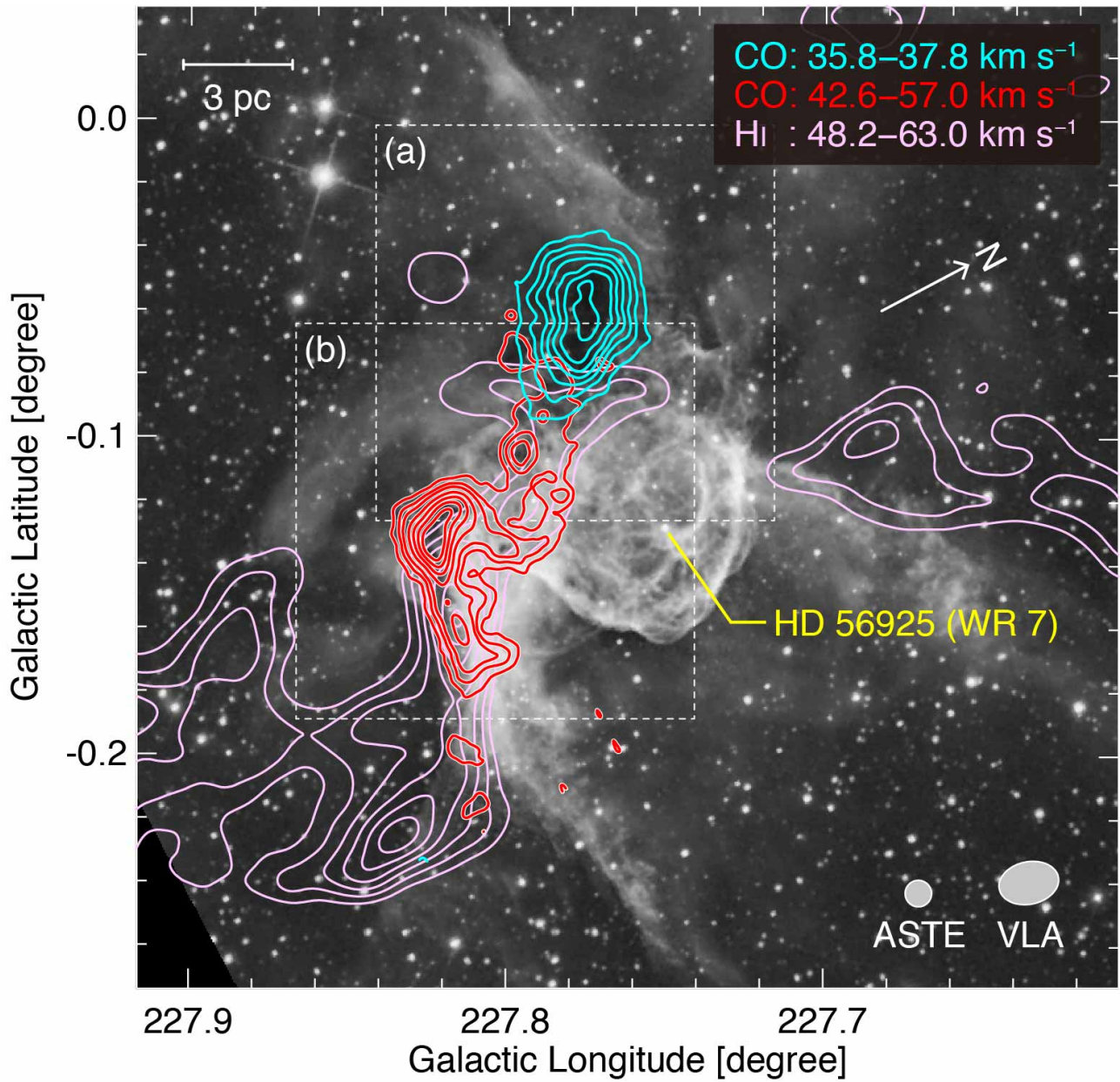


Fig. 5. Gray-scale optical image as shown in Figure 1, superposed with the $^{12}\text{CO}(J = 3-2)$ contours (red and blue) and HI contours (magenta, Cappa et al. 1999). The integrated velocity range is from 35.8 to 37.8 km s^{-1} for the blue-shifted CO cloud; from 42.6 to 57.0 km s^{-1} for the red-shifted CO cloud; from 48.2 to 63.0 km s^{-1} for the HI cloud. The contour levels are 1, 2, 3, 4, 5, 6, and 7 K km s^{-1} for the blue-shifted CO cloud; 3, 6, 9, 15, 21, 27, and 33 K km s^{-1} for the red-shifted CO cloud; 40, 60, 80, 100, 120, 140, and 160 K km s^{-1} for the HI clouds.

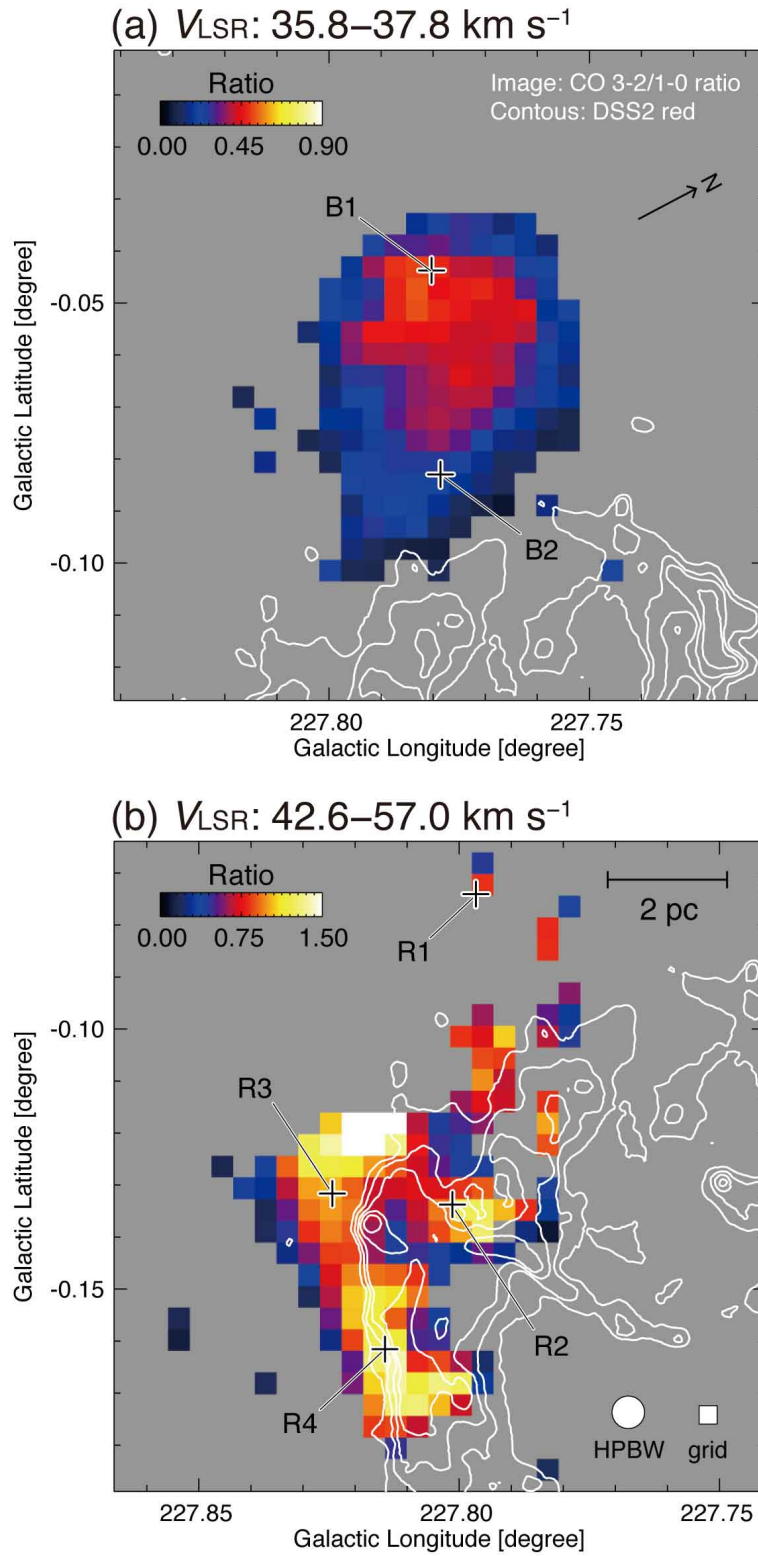


Fig. 6. Maps of $^{12}\text{CO } J = 3\text{--}2 / 1\text{--}0$ ratio toward the (a) blue-shifted CO cloud ($V_{\text{LSR}} = 35.8\text{--}37.8 \text{ km s}^{-1}$) and (b) red-shifted CO cloud ($V_{\text{LSR}} = 42.6\text{--}57.0 \text{ km s}^{-1}$), which represent the regions shown by dashed boxes in Figure 5. The white contours indicate the DSS2 red intensity. The velocity ranges of $^{12}\text{CO}(J = 3\text{--}2)$ are the same as Figures 5.

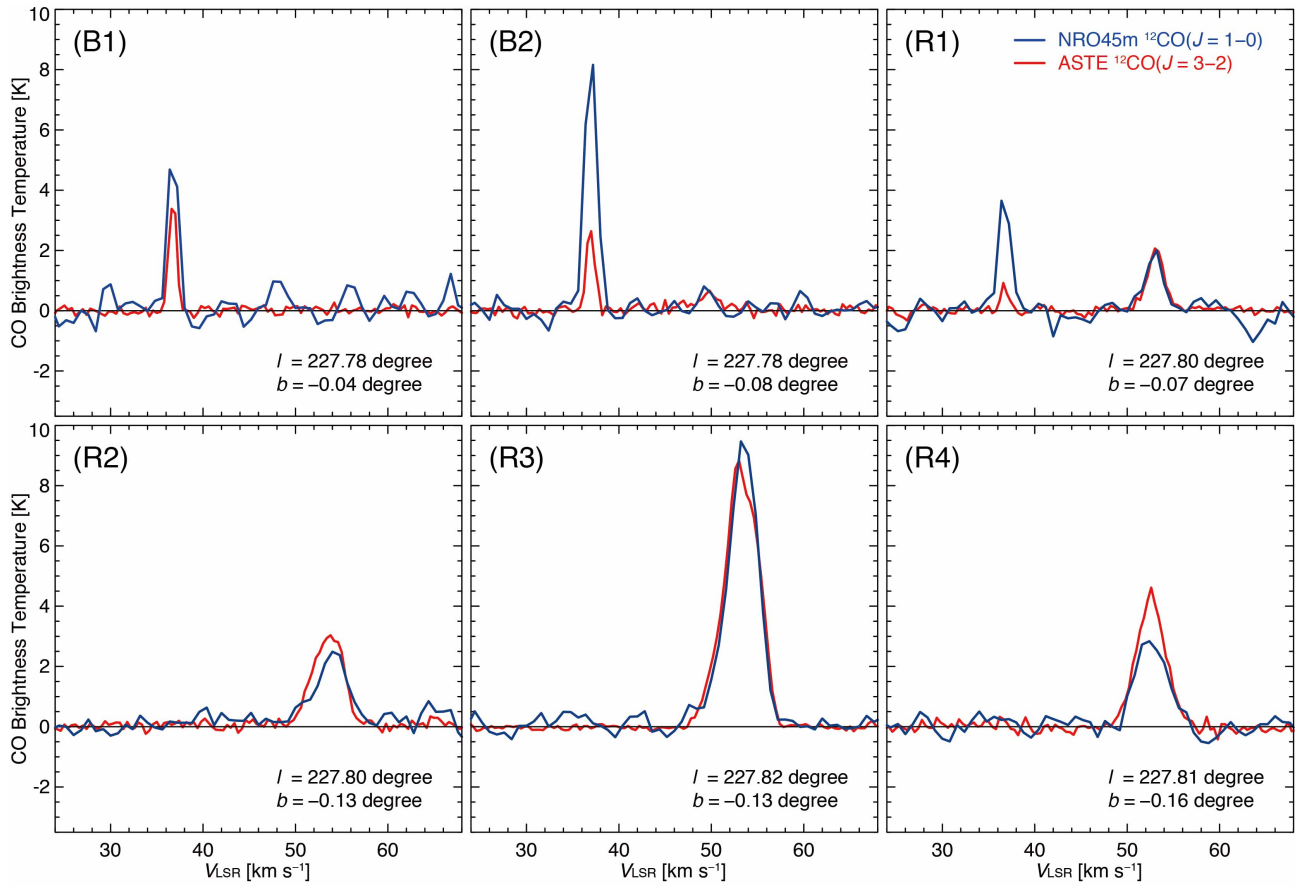


Fig. 7. Typical line profiles of ASTE $^{12}\text{CO}(J = 3-2)$ and NRO45 $^{12}\text{CO}(J = 1-0)$ for the regions B1 and B2 in the blue-shifted CO cloud and R1–R4 in the red-shifted CO cloud.

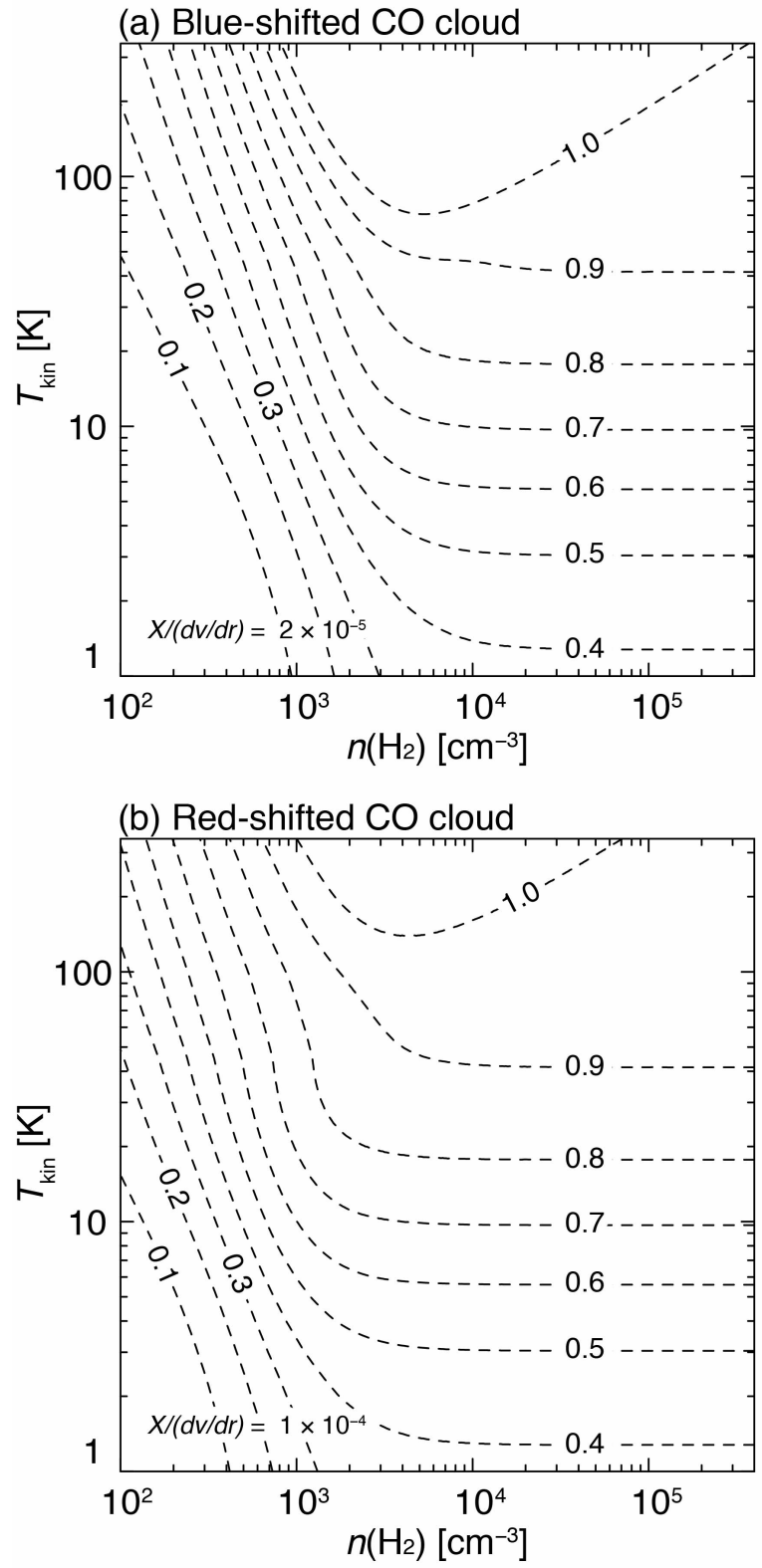


Fig. 8. LVG results on the number density $n(\text{H}_2)$ and kinematic temperature T_k plane for the (a) blue-shifted CO cloud and (b) red-shifted CO cloud (see text).

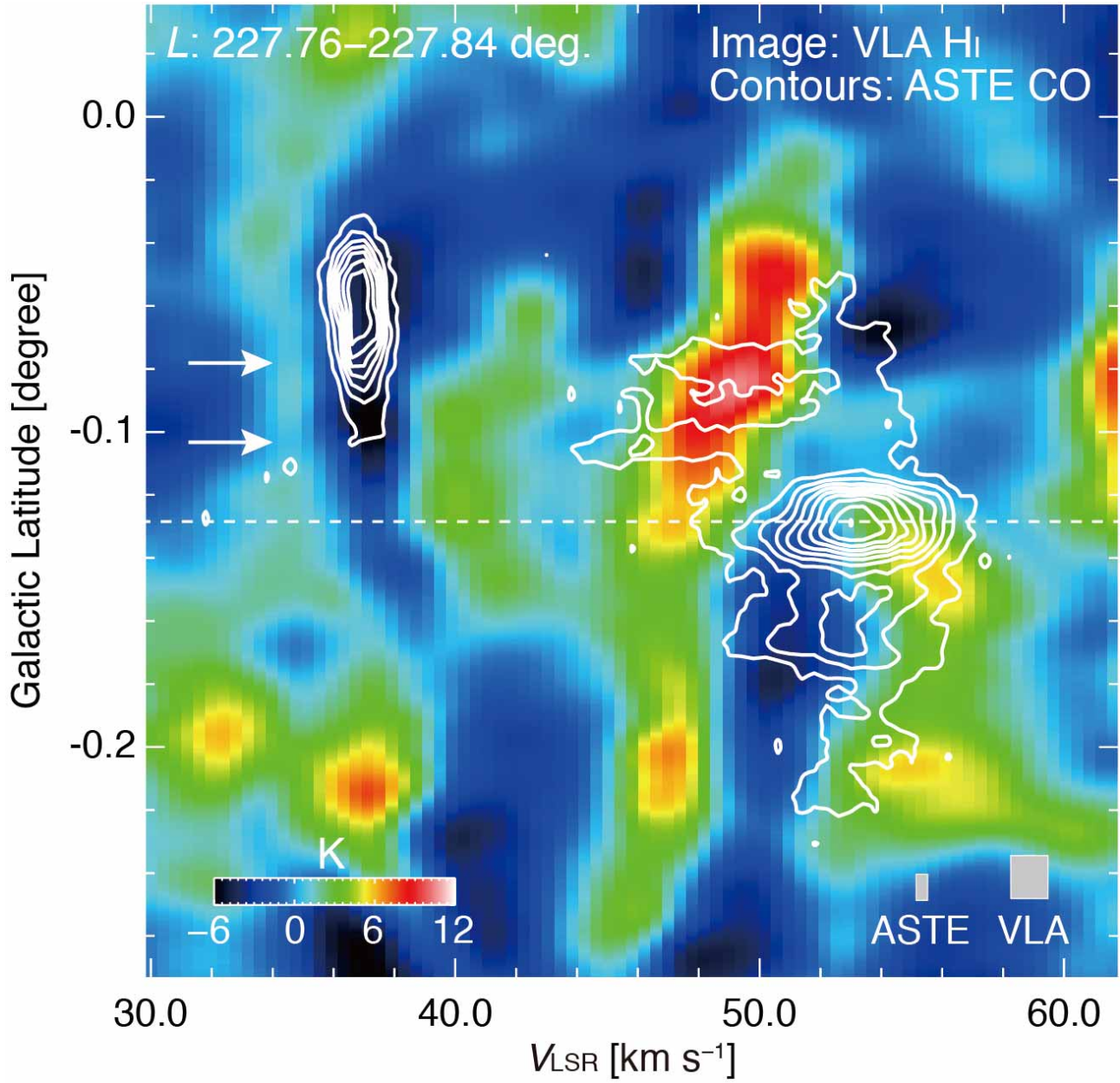


Fig. 9. Position-velocity diagram of the VLA H I superposed on the ASTE $^{12}\text{CO}(J = 3-2)$. The integration range of galactic latitude is from $227.^\circ 76$ to $227.^\circ 84$. The lowest contour level and intervals of $^{12}\text{CO}(J = 3-2)$ are 0.11 K and 0.23 K, respectively. The white arrows represent the directions of the bridging features seen in H I and CO. The dashed vertical line indicates a position of the WR star.

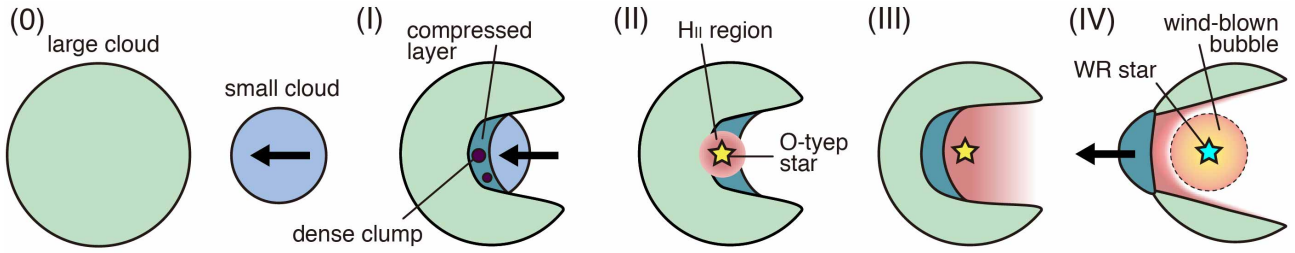


Fig. 10. Schematic illustrations of the cloud-cloud collision model presented by Habe & Ohta (1992) and by Torii et al. (2015), with minor modifications.

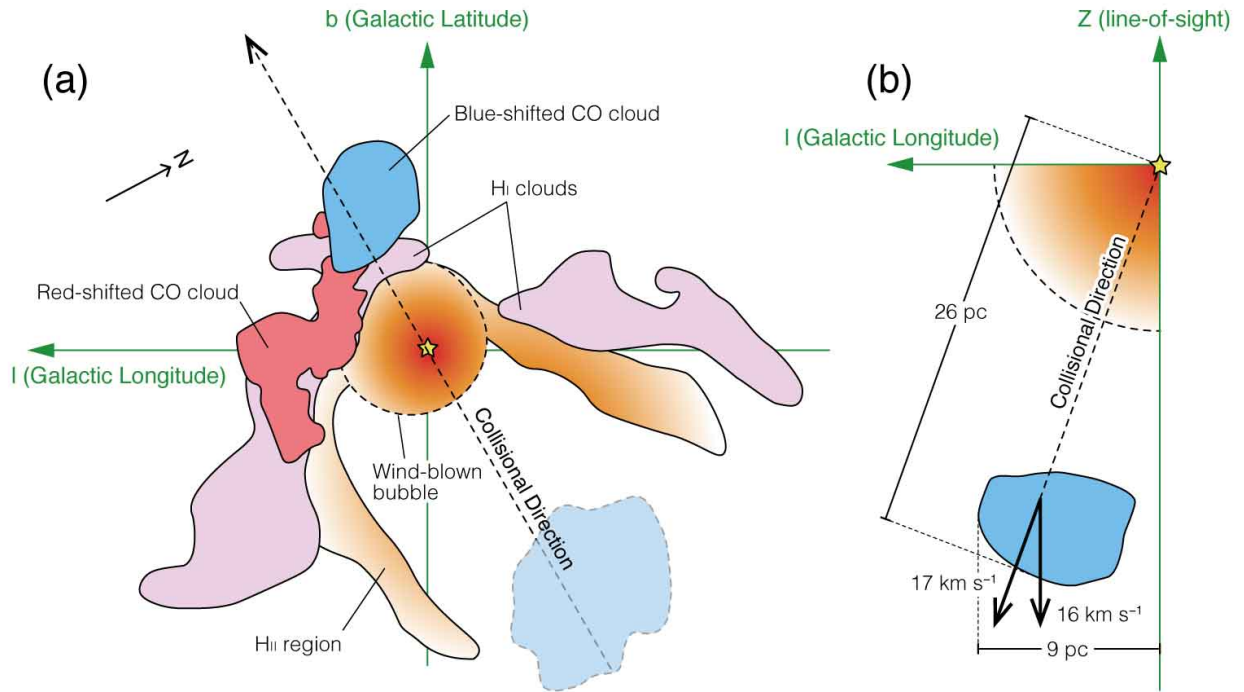


Fig. 11. Schematic illustrations of the cloud-cloud collision in NGC 2359 are presented on the l - b plane in (a) and l - z plane in (b), where the l - and b -axes are defined as Galactic longitude and latitude, respectively, and the z -axis represents to along the line-of-sight.